Research Article Vol. 15, No. 12 / 1 Dec 2024 / Biomedical Optics Express 6682
Biomedical Optics EXPRESS

Enhancing image reconstruction in photoacoustic imaging using spatial coherence mean-to-standard-deviation factor beamforming

XINSHENG WANG,[1] DAN WU,[1,4] YONGHUA XIE,[1] YUANYUAN BI,[1] YUNQING XU,[1] JING ZHANG,[1,2] QING LUO,[1] AND HUABEI JIANG[1,3,5]

[1]School of Optoelectronic, Chongqing University of Posts and Telecommunications, Chongqing, China
[2]Department of Ultrasound Imaging, The Fifth People's Hospital of Chengdu, Chengdu, China
[3]Department of Medical Engineering, University of South Florida, Tampa, FL 33620, USA
[4]wudan@cqupt.edu.cn
[5]hjiang1@usf.edu

Abstract: In photoacoustic imaging (PAI), a delay-and-sum (DAS) beamforming reconstruction algorithm is widely used due to its ease of implementation and fast execution. However, it is plagued by issues such as high sidelobe artifacts and low contrast, that significantly hinder the ability to differentiate various structures in the reconstructed images. In this study, we propose an adaptive weighting factor called spatial coherence mean-to-standard deviation factor (scMSF) in DAS, which is extended into the spatial frequency domain. By combining scMSF with a minimum variance (MV) algorithm, the clutter level is reduced, thereby enhancing the image contrast. Quantitative results obtained from the phantom experiment demonstrate that our proposed method improves contrast ratio (CR) by 30.15 dB and signal-to-noise ratio (SNR) by 8.62 dB compared to DAS while also improving full-width at half maxima (FWHM) by 56%. From the *in-vivo* experiments, the scMSF-based reconstruction image exhibits a higher generalized contrast-to-noise ratio (gCNR), indicating improved target detectability with a 25.6% enhancement over DAS and a 22.5% improvement over MV.

1. Introduction

Photoacoustic Imaging (PAI) is an advanced non-invasive imaging technique that integrates optical and acoustic technologies, which has garnered significant attention in the last two decades [1–3]. It utilizes the high contrast of optical imaging and the exceptional penetration depth of ultrasound (US) imaging to enable rendering of high optical contrast with scalable ultrasound resolution at considerable imaging depths [4–7]. Short laser pulses are used to excite biological tissues in PAI. Subsequently, due to the transient thermoelastic expansion of tissue chromophores, broadband ultrasound waves (known as photoacoustic signals) are generated. An ultrasound transducer receives and records these photoacoustic (PA) signals for PAI image reconstruction [8–10]. PAI can accurately capture endogenous chromophores in blood vessels, including oxygenated hemoglobin (HbO_2) and deoxygenated hemoglobin (HbR), owing to its sensitivity to these components. By analyzing these components, it evaluates blood oxygen saturation ($\%sO_2$), offering an effective indicator for assessing individual physiological status [11]. In recent years, PAI has been increasingly utilized in preclinical and clinical research domains including functional brain imaging [12–14], cardiovascular [15,16], breast cancer screening [17–19], and skin disease diagnosis [20–22].

Enhanced clarity and accuracy of PA images to more faithfully reflect the initial pressure distribution inside tissue is the primary goal pursued by current PA image reconstruction algorithms [23]. Several algorithms have been developed to optimize the quality of PA images [24–26]. Among these, Delay-and-sum (DAS) algorithm has gained popularity in both

#542710 https://doi.org/10.1364/BOE.542710
Journal © 2024 Received 20 Sep 2024; revised 12 Oct 2024; accepted 15 Oct 2024; published 5 Nov 2024

Biomedical Optics EXPRESS

photoacoustic and ultrasound imaging due to its simplicity and real-time processing capabilities [27]. However, DAS algorithm has several limitations, such as reduced spatial resolution, high sidelobe levels, low contrast and intense artifacts [28]. Extensive research has been conducted to address the inherent limitations of DAS beamforming algorithm. For example, variational coherence factor (VCF) [29], modify coherence factor (MCF) [30], lag-coherence factor (LCF) [31]. In 2015, Matrone et al. proposed a delay-multiply-and-sum (DMAS) algorithm based on signal correlation, which aims to overcome some of the limitations of DAS algorithm [32]. In 2017, the noise suppression limitations of DMAS algorithm were addressed by Matrone et al. through an enhanced version known as double-stage delay-multiply-and-sum (DS-DMAS) [33]. DS-DMAS significantly improved noise tolerance compared to DMAS, but it is computationally expensive than DMAS. Kirchner et al. proposed a signed delay-multiply-and-sum (sDMAS) algorithm, which better preserves low-frequency PA information than DMAS and demonstrated its applicability to multispectral PAI [34]. CF-DMAS has been proven to be effective in real-time clinical photoacoustic imaging of humans *in-vivo* [35]. Several improved DMAS algorithms and their integration with traditional beamformers have been previously reported [36,37]. The minimum variance (MV) adaptive beamforming algorithm is used to overcome the limitations of non-adaptive algorithms [38]. In addition, CF is used in MV algorithm to improve image quality [39]. Although MV algorithm faces challenges in real-time imaging due to its requirement for extensive and complex inverse matrix computations, researchers have developed methods to reduce its computational complexity. Short-lag spatial coherence (SLSC) [40] is another beamforming algorithm that can be used for PA and US imaging, demonstrating potential in applications such as visualization of brachytherapy seeds in prostate cancer treatment [41] and guidance of spinal pedicle cannulation [42], and mitigating skin tone bias [43]. However, SLSC discards signal amplitude information, making it unsuitable for quantitative imaging. Mora et al. proposed generalized spatial coherence (GSC) beamforming algorithm [44]. Compared to SLSC, this algorithm retains signal amplitude information while achieving better image quality.

In this paper, we propose a new adaptive weighing method named spatial coherence mean-to-standard-deviation factor (scMSF) and further combined it with MV beamforming algorithm to reduce the clutter level. In order to enhance the robustness of the algorithm, it is extended to the spatial frequency domain (fscMSF). The algorithm was validated through numerical simulations and phantom experiments, and quantitatively accessed using various image quality metrics. Furthermore, it was evaluated using PA data collected from human volunteers.

2. Materials and methods

2.1. Delay-and-sum and minimum variance beamforming

DAS algorithm is widely employed for time-domain reconstruction in PA imaging. In DAS, appropriate delays are applied to the detected signals by calculating the distance between each transducer element and the point of interest. The signals obtained from all the elements are summed to obtain the composite signal strength at particular pixel. Repeat this process for all pixels within the reconstruction area. The output of DAS (y_{DAS}) at pixel position p can be represented as [27]:

$$y_{DAS}(p) = \sum_{i=1}^{N} x_i[k + \Delta_i(p)], \tag{1}$$

where N represents the number of transducer elements, x_i is the PA signal is the PA signal intensity corresponding to the i^{th} element, k is time index, and Δ_i is the time delay corresponding to the i^{th} element. DAS has limited ability to reject off-axis interference signals, resulting in decreased image quality.

MV adaptive beamforming algorithm achieves off-axis signal suppression by minimizing the total output energy of the array [45]. The optimal weights vector of MV at point p, $\boldsymbol{w}_{mv}(p)$ are

Biomedical Optics EXPRESS

given by following equation:

$$\boldsymbol{w}_{mv}(p) = \frac{\boldsymbol{R}(p)^{-1}\boldsymbol{a}}{\boldsymbol{a}^{\boldsymbol{H}}\boldsymbol{R}(p)^{-1}\boldsymbol{a}} \tag{2}$$

where $\boldsymbol{R}(p)$ is the covariance matrix estimated using aperture data, $\boldsymbol{a}$ represents the directional vector, $(\cdot)^H$ donates the conjugate transpose. Before calculating the optical weights for MV, the received PA signals need to be appropriately delayed. Therefore, the directional vector becomes an array of ones [46]. Directly acquiring the covariance matrix is often impractical in practical applications. Therefore, it is typically estimated using aperture data. To make the covariance matrix more accurate, subarray averaging and temporal averaging techniques are used. The covariance matrix after averaging can be represented as:

$$\widehat{\boldsymbol{R}}(p) = \frac{1}{(2K+1)(N-L+1)} \times \sum_{n=-K}^{K} \sum_{l=1}^{N-L+1} X_l(k+n) X_l^H(k+n) \tag{3}$$

where L is the subarray length, and $2K+1$ is the axial points used for temporal averaging. $X_l = [x_l, x_{l+1}, \ldots, x_{l+L-1}]^T$ is the l^{th} subarray. To enhance the robustness of covariance matrix, diagonal loading (DL) techniques are used [47]. It is calculated as follows:

$$\hat{\boldsymbol{R}}_{DL}(p) = \hat{\boldsymbol{R}} + (\varepsilon \cdot trace\{\hat{\boldsymbol{R}}\})\boldsymbol{I} \tag{4}$$

where $\boldsymbol{I}$ is the identity matrix, $\varepsilon \cdot trace\{\hat{\boldsymbol{R}}\}$ is the diagonal loading factor, where ε is a constant, typically smaller than $1/L$. The output of MV is finally given as:

$$y_{MV}(p) = \frac{1}{N-L+1} \sum_{l=1}^{N-L+1} \boldsymbol{w}_{mv}^H X_l \tag{5}$$

2.2. Spatial coherence mean-to-standard-deviation factor

The numerator term of the mean-to-standard-deviation factor uses the mean of DAS, without accounting for spatial correlation. Therefore, in scMSF, the numerator term uses the mean of small aperture generalized spatial coherence (SA-GSC), and the denominator term uses the standard deviation of DAS. GSC can be represented as [44]:

$$\begin{aligned} y_{\mathrm{GSC}}(p) &= \sum_{m=1}^{M} \sum_{i=1}^{N-m} \frac{x_i(k)}{\sqrt[4]{\sum_{k=k_1}^{k_2} x_i^2(k)}} \cdot \frac{x_{i+m}(k)}{\sqrt[4]{\sum_{k=k_1}^{k_2} x_{i+m}^2(k)}} \\ &= \sum_{m=1}^{M} \sum_{i=1}^{N-m} S_i(k) \cdot S_{i+m}(k) \end{aligned} \tag{6}$$

where m is the lag. The kernel size ($\Delta k = k_2 - k_1$) is chosen at a single wavelength to achieve a balance between axial resolution and correlation stability. Eq. (6) can be written as:

$$\begin{aligned} y_{GSC}(p) = {} & (S_1S_2 + S_2S_3 + \cdots S_{N-2}S_{N-1} + S_{N-1}S_N) + (S_1S_3 + S_2S_4 + \cdots S_{N-2}S_N) \\ & + \cdots + (S_1S_{1+(M-1)} + S_2S_{2+(M-1)} + \cdots S_{N-(M-1)}S_N) \\ & + (S_1S_{1+M} + S_2S_{2+M} + \cdots S_{N-M}S_N) \end{aligned} \tag{7}$$

Biomedical Optics EXPRESS

Merge and sum polynomials in Eq. (7), it can be written as:

$$\begin{aligned}\hat{y}_{SA-GSC}(p) = &\underbrace{[S_1(S_2 + S_3 + \cdots + S_{1+M})]}_{frist\ term} + \underbrace{[S_2(S_3 + S_4 + \cdots + S_{2+M})]}_{\text{second } term} + \cdots + \\ &\underbrace{[S_{N-M}(S_{N-M+1} + S_{N-M+2} + \cdots + S_{N-M+M})]}_{(N-M)th\ term} + \cdots + \\ &\underbrace{[S_{N-2}(S_{N-1} + S_N)]}_{(N-2)th\ term} + \underbrace{[S_{N-1}S_N]}_{(N-1)th\ term}\end{aligned} \tag{8}$$

In Eq. (8), the auto-correlation of the same signal with different lag signals is combined into a new beamforming term. Each term can be considered as a form of small aperture DAS. The newly generated term can be expressed as:

$$\hat{S}_p = \sum_{j=i+1}^{\min(i+M,N)} S_j,\ for\ 1 \le i \le N-1, \tag{9}$$

Therefore, Eq. (8) can be written as:

$$\hat{y}_{SA-GSC}(p) = \sum_{i=1}^{N-1} \hat{S}_i \tag{10}$$

In this work, we propose to use the mean of above SA-GSC algorithm as the numerator term in the weighing factor. Considering that in DAS, the aperture data for the target region has a low standard deviation, while the aperture data for the background noise region has a high standard deviation. The standard deviation corresponding to the background noise region is significantly higher than that of the target region. Therefore, the standard deviation from DAS is used as the denominator of the weighting factor. At this point, the target region has a high mean and low standard deviation, resulting in a high weighting value. In contrast, the background region has a high mean and high standard deviation, leading to a low weighting value. Thus, scMSF can be defined as:

$$y_{scMSF}(p) = \frac{\frac{1}{N-1}\sum_{i=1}^{N-1} \hat{S}_i}{\sqrt{\frac{1}{N}\sum_{i=1}^{N}(x_i - \frac{1}{N}\sum_{i=1}^{N} x_i)}^2}, \tag{11}$$

Since the Fourier transform can separate coherent and incoherent components from aperture data, we utilize this property to compute scMSF in the frequency domain. This aims to improve the algorithm's adaptability and robustness to signal variations. fscMSF can be represented as:

$$y_{fscMSF}(p) = \frac{\frac{1}{N-1}\sum_{i=1}^{N-1}(\hat{s}_1 - \hat{s}_i)}{\sqrt{\frac{1}{N}\sum_{i=1}^{N}[(s_1' - s_i') - \frac{1}{N}\sum_{i=1}^{N}(s_1' - s_i')]^2}}, \tag{12}$$

where $\hat{s}_1$ is the DC component of SA-GSC aperture, s_1' is the DC component of DAS aperture. After $y_{fscMSF}(p)$ is calculated, the fscMSF is used to weight the DAS and MV, which can be represented as follows:

$$y_{fscMSF+DAS}(p) = y_{fscMSF}(p) \times y_{DAS}(p), \tag{13}$$

$$y_{fscMSF+MV}(p) = y_{fscMSF}(p) \times y_{MV}(p). \tag{14}$$

Biomedical Optics EXPRESS

2.3. PAI system

The efficacy of our proposed method was further validated using phantom and *in-vivo* experiments through a home-made real-time PAI system. A schematic diagram of our PAI system is shown in Fig. 1. High-frequency OPO pulsed laser (SpitLight EVO S OPO, Innolas, Justus-von-Liebig Ring 8, 82152 Krailling, Germany) with a pulse repetition frequency (PRF) of 100 Hz, a pulse width of 5 ns, and a wavelength of 760 nm is the excitation source for phantom and *in-vivo* experiments. The optical energy density of the laser beam was maintained at approximately 2 mJ/cm^2, significantly lower than the FDA's safety threshold of 22 mJ/cm^2, ensuring the safety of the experiments. After the laser was directed onto the object through an optical fiber, PA signals are obtained by a self-constructed 256-channel semi-annular ultrasonic transducer, with the transducer's center frequency being 5 MHz and a curvature radius of 80 mm. The PA signals collected by the transducer was amplified and filtered by the data acquisition (DAQ) system with a sampling rate of 40 MHz and a gain of 80 dB, followed by real-time PA imaging using the DAS algorithm. All beamforming processing is performed on a desktop computer with an Intel Core i5-13600KF CPU at 5.1 GHz and 32 GB of RAM.

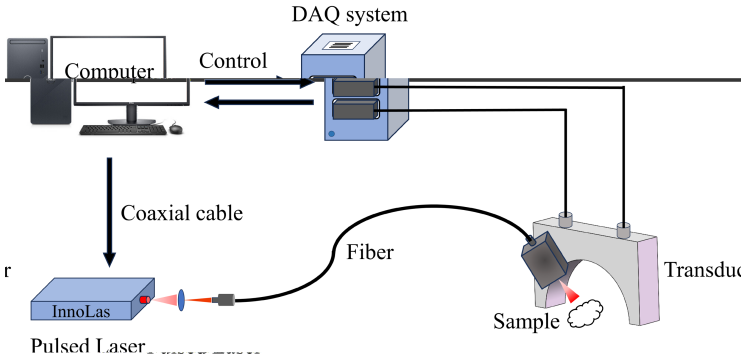

Fig. 1. The schematic diagram of PAI system.

2.4. Numerical simulations

Numerical simulations were designed to compare our proposed algorithm with the existing algorithm (i.e., DAS and MV). All numerical simulation studies were conduct using the k-Wave MATLAB toolbox [48]. In our simulation study, we selected a uniform propagation medium with a constant sound speed of 1500 *m/s* and a medium density of 1040 kg/m^3 as the propagation environment. Five pairs of circular point absorbers with a radius of 0.1 mm were placed in the aforementioned propagation environment. These absorbers were vertically positioned at five different depth levels: 10 mm, 13 mm, 16 mm, 19 mm, and 22 mm. Adjacent targets in the lateral direction are spaced 2 mm apart. A 128-channel semi-annular transducer with a curvature radius of 6 mm was used to detect the PA signals. The distance between the bottom of the semi-annular transducer and the first circular point absorber was 10 mm. The center frequency of the transducer was 7.5 MHz. The PA signal was recorded at a sampling frequency of 50 MHz. Imaging field of view (FOV) was 45×13 mm^2. During the simulation, Gaussian white noise with a SNR of 30 dB was added to each captured PA signals.

2.5. Phantom and in-vivo experiments

The performance of the proposed algorithm was validated through two phantom experiments. Figure 2(a) illustrates a schematic of phantom 1. Six black nylon lines (0.1 mm) are placed as PA absorbers in pairs within a water tank and positioned vertically to the ultrasonic transducer,

Biomedical Optics EXPRESS

with later spacings of 10 mm, 20 mm, and 30 mm. Figure 2(b) illustrates a schematic of phantom 2, with three black nylon lines (1 mm) positioned at varying depths within the water tank. For *in-vivo* experiments, we validated the index finger and the right palm of human volunteer using an ultrasonic transducer wrapped in a water-filled, translucent plastic sheet (TPU) with transabdominal ultrasound characteristics. Human volunteer is in contact with the TPU. Ultrasound coupling agent was applied to the human volunteer for maximizing ultrasound transmission.

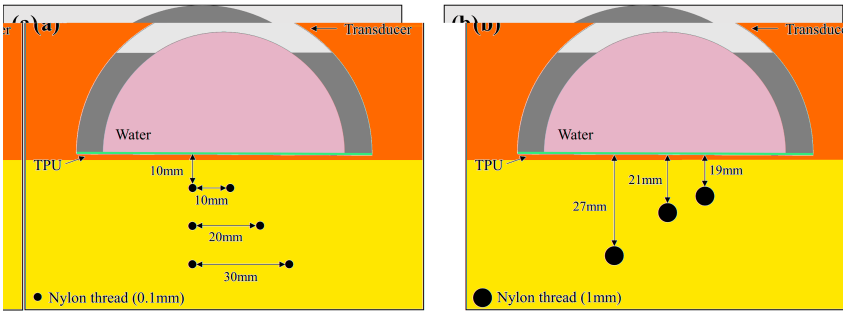

Fig. 2. (a) the schematic diagram of phantom 1. (b) the schematic diagram of phantom 2.

2.6. Quantitative assessment of reconstructed images

Full-width at half maxima (FWHM), contrast ratio (CR), signal-to-noise ratio (SNR) and generalized contrast-to-noise ratio (gCNR) were used to quantitatively evaluate image quality, and they defined as follows [31,49]:

$$CR = 20\log_{10}(\frac{\mu_{in}}{\mu_{out}}), \tag{15}$$

$$SNR = 20\log_{10}(\frac{\mu_{in}}{\sigma_{out}}), \tag{16}$$

$$gCNR = 1 - \sum_{x=0}^{1} \min\{h_{in}(x), h_{out}(x)\}, \tag{17}$$

where, μ_{in} and μ_{out} denote the average PA signal values within the region of interest (ROI) and the background noise region, respectively. σ_{out} represents the standard deviation of the PA signal in the background noise region. h_{in} and h_{out} represent the probability density functions of the PA signal amplitudes in the ROI and background noise regions, respectively.

3. Results and discussion

3.1. Numerical simulations

The reconstructed images of the 10 point targets using different reconstruction algorithms (DAS, MV, fscMSF-DAS, and fscMSF-MV) are shown in Fig. 3. All images are presented with the same dynamic range. For fscMSF-DAS and fscMSF-MV, the lag was selected as 30% of the transducer aperture. The ground-truth image of the numerical simulation is depicted in Fig. 3(a). Figure 3(b) and (c) represent the reconstructed images of DAS and MV, respectively. The reconstructed images of our proposed algorithm weighting DAS and MV are presented in Fig. 3(d) and Fig. 3(e), denoted as fscMSF-DAS and fscMSF-MV, respectively. In Fig. 3(b), PA image reconstructed using DAS are characterized by wide mainlobe and strong sidelobes.

Biomedical Optics EXPRESS

Additionally, due to the mutual interference of the sidelobes of two adjacent absorbers, significant artifacts are generated between the absorbers. As the imaging depth is increased, the point targets in DAS gradually became barely detectable. As shown in Fig. 3(c), although the MV algorithm attenuates the sidelobes to some extent, fails to sufficiently reduce their magnitude. The fscMSF weighting significantly suppresses the sidelobes and artifacts between absorbers in DAS and MV beamformed images, providing narrower mainlobe and enabling the detection of point targets at greater depths, as shown in Fig. 3(d) and (e).

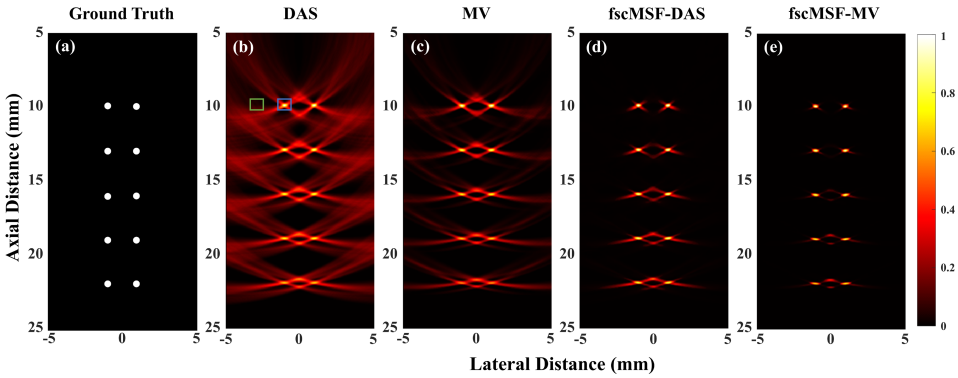

Fig. 3. The numerical simulation results. (a)Ground-truth image of numerical point phantom. Employed the following four different algorithms for image reconstruction: (b) DAS, (c) MV, (d) fscMSF-DAS, and (e) fscMSF-MV, to reconstruct images of 10 simulated point targets.

To better compare the reconstructed images, Figs. 4(a) and 4(b) show the lateral distribution of PA signals intensity at depths of 13 mm and 19 mm, respectively. The average of the FWHM value of the two targets at the same depth is taken as the final FWHM value at that depth. The variation of the FWHM of the point targets with increasing depth is depicted in Fig. 4(c). The results indicate that, compared to traditional beamforming algorithms, the fscMSF-MV algorithm exhibits the greatest sidelobes suppression and the narrowest mainlobe width. As the imaging depth increases, the resolution of all algorithms decreases. However, compared to DAS and MV, the resolution is significantly enhanced after fscMSF weighting. At a depth of 22 mm, the FWHM values of the point targets for DAS, MV, fscMSF-DAS, and fscMSF-MV are 0.90 mm, 0.85 mm, 0.49 mm, and 0.48 mm, respectively. Therefore, our proposed algorithm significantly enhances lateral spatial resolution compared to DAS and MV.

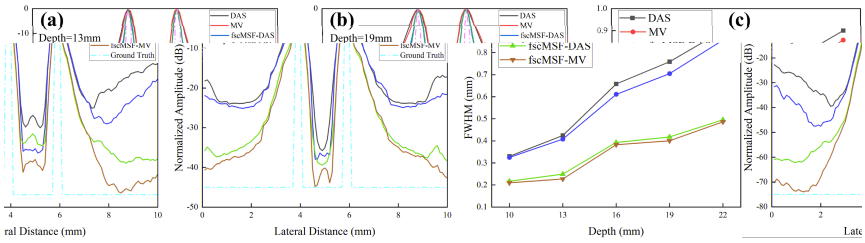

Fig. 4. (a) and (b) show the lateral distribution of PA signal for point targets at depths of 13 mm and 19 mm, respectively. (c) displays the FWHM of reconstructed point targets at different depths.

To evaluate the efficacy of different reconstruction algorithms, we quantitatively calculated the CR and SNR for all the recovered targets. When calculating the CR and SNR for the point

Biomedical Optics EXPRESS

targets at a depth of 10 mm, we selected regions based on the markings in Fig. 3(b): the target region delineated by the blue box represents the imaging area of the point targets, while the green box delineates the background noise region. The background region and the target region are at the same depth. For point targets at other depths, we applied the same criteria as those used for the 10 mm depth targets to select the target and background regions. Figure 5(a) and Fig. 5(b) respectively illustrate the CR and SNR values for all algorithms at five different depths. These values were obtained by averaging the measurements of two targets at each depth to ensure the accuracy of the results. From the Fig. 5, it is clear that our proposed algorithm significantly improves both CR and SNR. Taking the example of point targets at a depth of 22 mm, the achievable CR values for DAS, MV, fscMSF-DAS, and fscMSF-MV are 10.28, 15.78, 23.92, and 27.43 dB, respectively. the achievable SNR values are 23.33, 26.38, 36.28, and 40.79 dB, respectively. The fscMSF-MV algorithm demonstrates a significant improvement in both CR and SNR, with an increase of at least 17 dB and 14 dB respectively, across all depths.

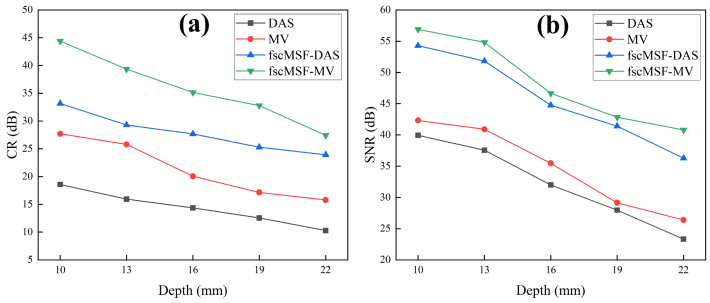

Fig. 5. Quantitative evaluation of the reconstructed images shown in Fig. 3: (a) depicts the CR values of point targets at various depths, while (b) illustrates the SNR values of point targets at different depths.

3.2. *Phantom experiments*

The PA results of two phantom experiments reconstructed using all beamforming algorithms are shown in Fig. 6 and Fig. 9, respectively. Figure 6(a1)-(d1) depict the PA images reconstructed using the DAS, MV, fscMSF-DAS, and fscMSF-MV algorithms for three pairs of 0.1 mm nylon lines, respectively, and displayed with the same dynamic range. For fscMSF-DAS and fscMSF-MV, the lag was selected as 30% of the transducer aperture. Figure 6(a2)-(d2) shows the local magnified images of the nylon threat phantom within the green box area in the reconstructed images by all algorithms. Each target in the phantom is clearly visible in all four reconstruction scenarios. However, when using the DAS algorithm, both the background noise and sidelobe artifacts are higher levels. After applying fscMSF weighting, the background noise nearly disappears, sidelobes and artifacts are suppressed to a lower level, and the detectability of targets is significantly improved. Figure 7(a) show the lateral variations in PA signal intensity for point targets at depth of 20 mm. The average of the FWHM values of the two targets at the same depth is taken as the final FWHM at that depth. Figure 7(b) displays the change in lateral resolution of targets reconstructed all algorithms as depth increases. Figure 7(a) demonstrates that after applying fscMSF weighting technique, the mainlobe becomes narrower and the sidelobes are significantly reduced. According to Fig. 7(b), the FWHM calculated at 10 mm for DAS, MV, fscMSF-DAS, and fscMSF-MV are 0.25 mm, 0.24 mm, 0.12 mm, and 0.11 mm. The FWHM of fscMSF-MV improved by 56.00% and 54.17% compared to DAS and MV, respectively. It indicates that the proposed fscMSF weighing method can achieve enhanced lateral resolution.

The quantitative evaluation of targets at different depths in phantom 1 was conducted using three image quality metrics: CR, SNR, and gCNR. The results of quantitative evaluation are

Biomedical Optics EXPRESS

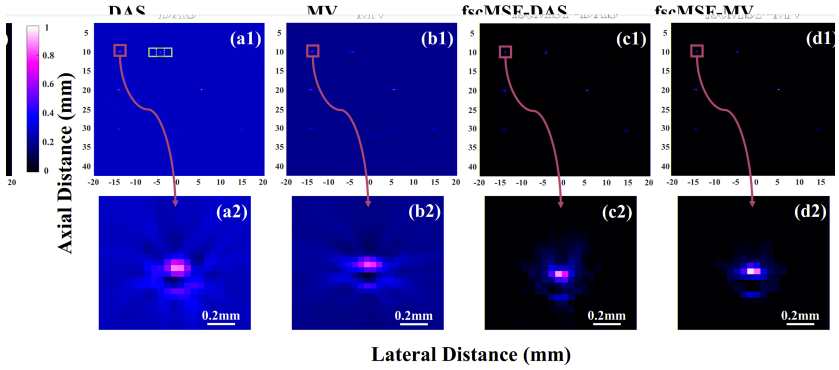

Fig. 6. PA images of phantom 1 were reconstructed using the (a1) DAS, (b1) MV, (c1) fscMSF-DAS, and (d1) fscMSF-MV algorithms. (a2)-(d2) show magnified images (marked with a green box) of the phantom at 10 mm reconstructed by different algorithms.

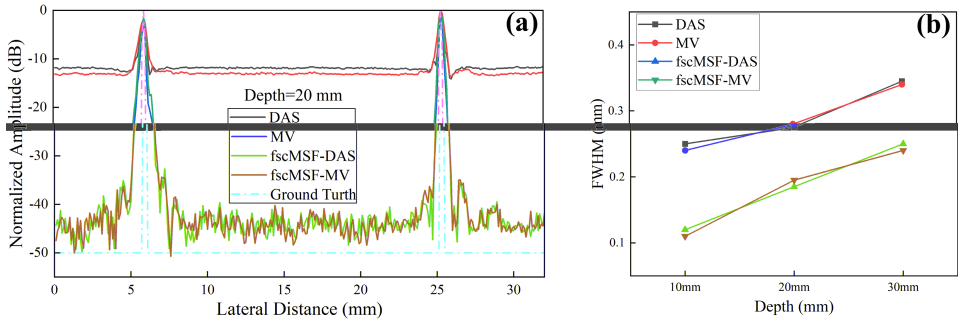

Fig. 7. (a) shows the variation in lateral PA energy intensity at a depth of 20 mm. (b) shows the change in FWHM of targets reconstructed by all algorithms as depth increases.

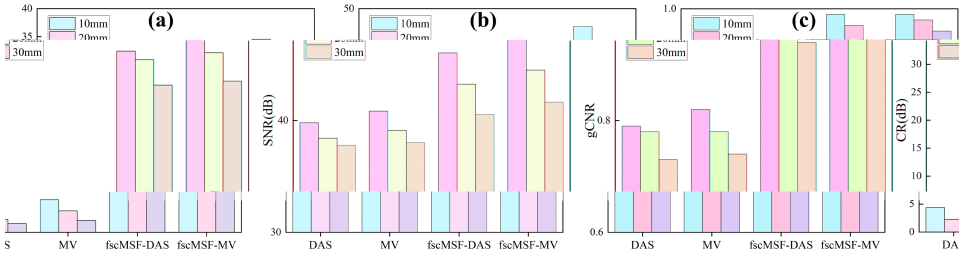

Fig. 8. All the algorithms were quantitatively evaluated at different depths in phantom 1 using (a) CR, (b) SNR, and (c) gCNR.

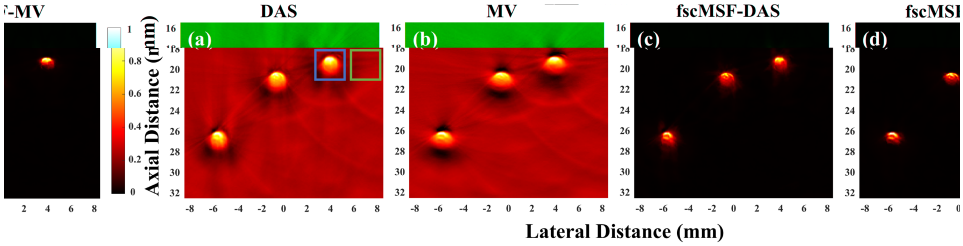

Fig. 9. Reconstructed PA images of phantom 2 using the following algorithms: (a) DAS, (b) MV, (c) fscMSF-DAS, and (d) fscMSF-MV.

Biomedical Optics EXPRESS

depicted in Fig. 8(a)-(c). The target region and background region are represented by blue and white boxes, respectively. The values of CR and SNR of DAS and MV are improved by incorporating the fscMSF weighting method, as shown in Fig. 8(a)-(b). Figure 8(c) demonstrates that although the gCNR of all algorithms decreases with increasing depth, the gCNR after fscMSF weighting consistently remains at a higher level.

The first phantom experiment demonstrates a significant enhancement in resolution and contrast ratio for multiple small targets through the proposed method. Considering that artifacts from large absorbers are significantly stronger than those from small ones, another phantom experiment was utilized to confirm the proposed method is effective in improving the imaging quality of large absorbers. Figure 9(a)-(d) depict the PA images reconstructed using the DAS, MV, fscMSF-DAS, and fscMSF-MV beamforming algorithms for three 1 mm nylon lines, respectively, and displayed with the same dynamic range. In the DAS image, there are noticeable streaking artifacts around point targets and high signal amplitude in the background. After applying fscMSF weighting, the streaking artifacts are significantly reduced, and the background noise is substantially lowered. In the fscMSF-MV image, the streaking artifacts and background noise are almost completely absent. We conducted quantitative evaluations of targets at 19 mm and 27 mm depths in Fig. 9, as shown in Fig. 10(a)-(c). At 19 mm depth, the fscMSF-MV algorithm improved CR and SNR relative to DAS by 23.48 dB and 9.98 dB, respectively. For gCNR, the fscMSF-MV algorithm improved by 15.1% relative to DAS and 13.8% relative to MV. It indicates that fscMSF weighting can provide better detectability of targets.

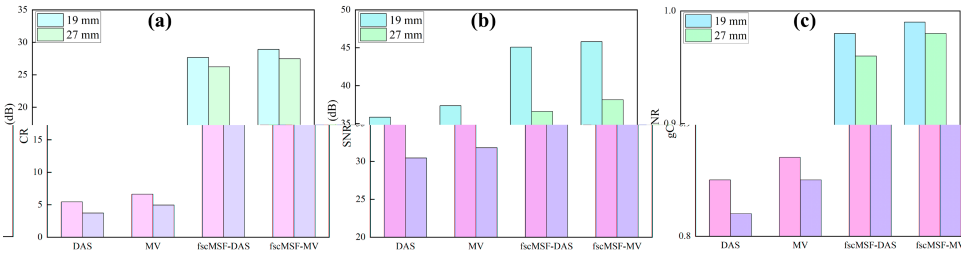

Fig. 10. Quantitative evaluation of the existing imaging algorithms (DAS and MV) and the proposed methods (fscMSF-DAS and fscMSF-MV): (a) CR, (b) SNR, and (c) gCNR of targets at two different imaging depths (19 mm and 29 mm).

3.3. *In-vivo experiments in human volunteers*

To assess the performance of our proposed reconstruction algorithm on *in-vivo* imaging, we used the PAI system to acquire PA data from the index finger and right palm of human volunteers and reconstructed PA images using all beamforming algorithms. Figures 11(a)–11(d) depict the PA images of the index finger reconstructed using the DAS, MV, fscMSF-DAS, and fscMSF-MV beamforming algorithms. For fscMSF-DAS and fscMSF-MV, the lag was selected as 30% of the transducer aperture. In the result reconstructed using the fscMSF-MV algorithm, the artifacts on the upper surface of the skin have almost completely disappeared. After fscMSF weighting, the layers of the skin can be clearly observed, making the dermis and epidermis of the finger skin more distinct and easier to differentiate (see the white arrows in Figs. 11(a)–11(d)). The background noise around the skin is significantly reduced after being weighed by fscMSF. The background noise weighted by the MV algorithm is lower than that weighed by the DAS algorithm (compare areas within the dashed circular boxes in Figs. 11(a)–11(d)). The lower background noise enhances the PA images contrast. Select the palmar digital veins within the blue box area in Fig. 11(a) as the target region for quantitative analysis. As shown in Table 1, compared to DAS, the fscMSF-MV algorithm improves the CR and SNR by 21.51 dB and 8.5 dB, respectively.

Biomedical Optics EXPRESS

When compared to MV, the CR and SNR are improved by 21.06 dB and 7.88 dB, respectively. When compared to DAS and MV, the fscMSF-MV algorithm improves the gCNR by 8.8% and 6.5%, respectively.

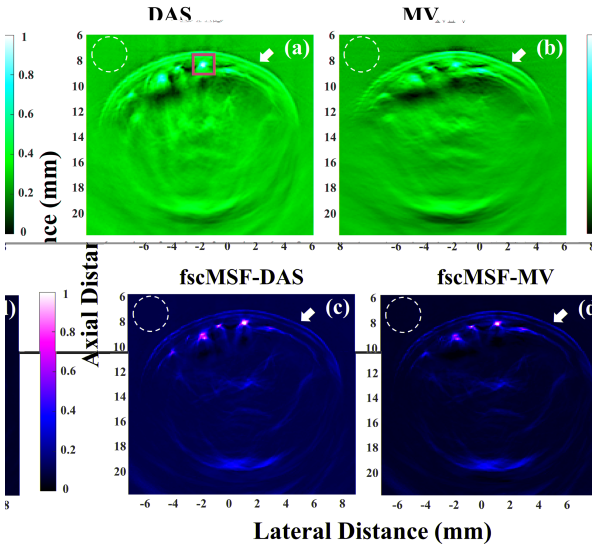

Fig. 11. Reconstructed PA images of the index finger obtained using (a) DAS, (b) MV, (c) fscMSF-DAS, and (d) fscMSF-MV.

Table 1. The imaging performance (SNR, CR, and gCNR) of different beamforming methods when imaging the palmar digital vein of the index finger.

	DAS	MV	fscMSF-DAS	fscMSF-MV
CR (dB)	5.42	5.87	26.34	26.93
SNR (dB)	39.72	40.34	47.75	48.22
gCNR	0.91	0.93	0.99	0.99

To further validate the efficacy of the proposed algorithm and assess its performance in enhancing the quality of superficial blood vessel visualization, we performed imaging on the right palm of a human volunteer. Figure 12(a) show the photography of the right palm, and the red dashed line is the location of the PA image region. Figure 12(b)-(e) show the PA images of the right palm reconstructed using four different algorithms: DAS, MV, fscMSF-DAS, and fscMSF-MV. In Fig. 12(b), Blood vessels respectively are one of the deep dorsal metacarpal veins (label 1) and ulnar vein deep palmar branch (label 2). After applying fscMSF weighting, the layered structure of skin becomes clearer (marked with white arrows in Fig. 12(b)-(e)). This result is consistent with the qualitative analysis of the index finger. When using our proposed method, the improvements in CR and SNR are clearly visible, which is due to the significant reduction in background noise. When using the conventional DAS algorithm (Fig. 12(b)), vessel contrast is low due to background noise and sidelobe artifacts. In the PA image reconstructed using the MV algorithm, background noise has been suppressed but remains strong. After weighting DAS and MV with fscMSF, the background noise in the PA images is significantly suppressed (see the dashed rectangular boxes in Figs. 12(b)–12(e)). Moreover, as the background noise decreases, blood vessels that were previously hidden due to strong noise become clearly visible in the PA images. When using the fscMSF-MV algorithm (Fig. 12(e)), background noise is suppressed, and vessel contrast is significantly enhanced.

Biomedical Optics EXPRESS

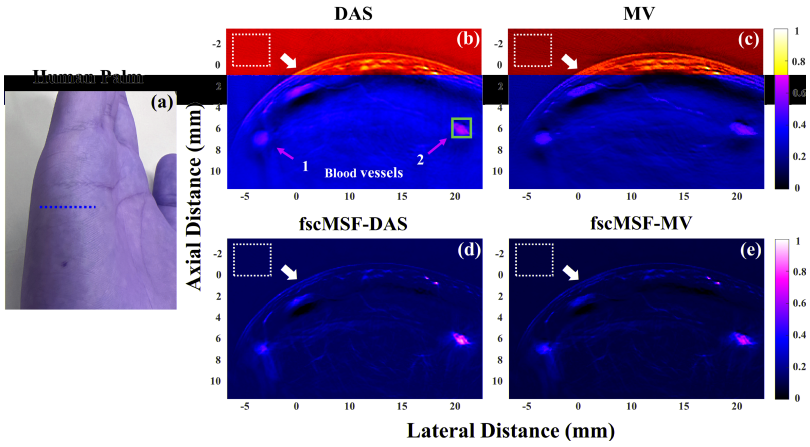

Fig. 12. The *in-vivo* experiment results of the right palm of a human volunteer. (a) a photograph of the right palm. The red dashed line indicates the location of the imaging region cross-section. The PA reconstruction images of the right palm of a human volunteer obtained using (a) DAS, (b) MV, (c) fscMSF-DAS, and (d) fscMSF-MV.

To quantitatively evaluate the improvement in PA image quality, we selected target and background regions to calculate the CR, SNR, and gCNR of one of the deep dorsal metacarpal veins (label 1) and ulnar vein deep palmar branch (label 2). In case of vessel 2, the target region is represented by the blue box in Fig. 12(b). The selection criteria for the vessel 1 are the same. In case of ulnar vein deep palmar branch, the CR values are 4.69 dB, 5.29 dB, 27.58 dB, and 29.07 dB for DAS, MV, fscMSF-DAS, and fscMSF-MV, respectively. The PA reconstruction image by fscMSF-MV improved the CR value by 24.38 dB and 23.78 dB compared to DAS and MV, respectively. And the SNR value relative to DAS and MV is improved by 9.22 dB and 8.85 dB, respectively. Regarding gCNR, our proposed algorithm achieves improvements of 13.8% and 12.5% compared to DAS and MV, respectively. When using our proposed method, there are significant improvements in CR, SNR, and gCNR for two vessels (more details can be found in Table 2).

Table 2. The measured quantitative values of different beamforming methods when imaging the palmar venous plexus of right palm

Blood vessel	DAS	MV	fscMSF-DAS	fscMSF-MV
CR (dB)				
1	4.08	4.79	24.77	25.46
2	4.69	5.29	27.58	29.07
SNR (dB)				
1	32.43	33.84	39.28	39.83
2	35.65	36.02	44.50	44.87
gCNR				
1	0.78	0.80	0.96	0.98
2	0.87	0.88	0.98	0.99

Biomedical Optics EXPRESS

4. Conclusion

In this work, we describe a weighted factor based on spatial coherence mean-standard deviation method to enhance the performance of PA imaging. The algorithm is extended to the frequency domain to enhance its robustness across different environments. The MV algorithm mitigates clutter by estimating the optimal weights for channel signals, thereby reducing off-axis energy. The fscMSF weighing factor is applied to the MV beamformer to enhance imaging contrast. Traditional DAS algorithm, due to its blindness and nonadaptiveness, result in reconstructed PA images with low resolution, high sidelobes, and poor CR value. Our proposed method effectively mitigates these drawbacks and provides improvements in image quality metrics such as higher resolution, sidelobe suppression, and contrast enhancement. The numerical simulation, phantom experiments, and *in-vivo* studies were used to validate the efficacy of the proposed method. The results of numerical simulation demonstrate that our proposed method outperforms the traditional methods in terms of FWHM, CR, and SNR (see Figs. 4 and 5). The results of the lateral energy distribution in the first phantom experiment show that our proposed method achieves lower sidelobe level and an FWHM closer to the phantom size (see Fig. 7). For the FWHM of the phantom at a depth of 10 mm, the fscMSF-weighted DAS and MV algorithms improve by 52% and 54%, respectively, compared to the algorithms without fscMSF weighting. Additionally, the quantitative evaluation results from the two phantom experiments indicate that the fscMSF-weighed PA images show significant improvements in CR, SNR, and gCNR compared to unweighted images (see Figs. 8 and 10). For the phantom at a depth of 19 mm in the second phantom experiment, the fscMSF-weighed CR and SNR increased by 22.3 dB and 8.44 dB, respectively. Although CR and SNR values decrease with depth, the fscMSF-weighed images still exhibition high CR and SNR values. *In-vivo* feasibility of fscMSF beamformers was demonstrated by performing PA imaging of the index finger and right palm of the human volunteer. The PA reconstruction results from the *in-vivo* experiments show that our proposed method enhances the clarity of the imaging region in PA images by reducing background noise (see Figs. 11 and 12). After fscMSF weighting, the skin structure in the index finger and right palm becomes more clearly visible, allowing for the distinct identification of the dermis and epidermis layers. The quantitative analysis of blood vessels in the index finger and right palm shows that the evaluation metrics of the fscMSF-weighed images are significantly improved compared to the unweighted images (see Tables 1 and 2). The CR/SNR values from the *in-vivo* experiments show that the fscMSF-MV algorithm improves by at least 20 dB and 6 dB, respectively, compared to the MV algorithm. For the deep dorsal metacarpal veins (label 1), the fscMSF-MV algorithm increases the gCNR by 0.18 compared to the MV algorithm, indicating a 22.5% improvement in lesion detectability.

Finally, all the experiment results demonstrate that our proposed method effectively enhances the clarity and details of PA images, with significant improvement in various quantitative image evaluation metrics. Furthermore, this method can be integrated with other beamforming algorithms to achieve even better PA imaging results.

In this study, we designed a novel weighting technique (fscMSF) aimed at overcoming the inherent limitations of traditional reconstruction algorithms, such as low resolution. This technique addresses issues such as insufficient contrast, prominent background noise, and low resolution typically associated with traditional algorithms. We comprehensively validated the efficacy of the proposed method through numerical simulations, phantom experiments, and *in-vivo* studies. The experimental results obtained have confirmed the efficacy of our proposed method in improving quantitative metrics including FWHM, CR, SNR, and gCNR.

Funding. State Key Laboratory of Trauma and Chemical Poisoning (SKLKF202205); Chongqing post doctoral research project (Nos 2021XM3040).

Acknowledgments. The authors of this paper wish to express their sincere appreciation and gratitude to the study participants of the cohort for donating their time.

Biomedical Optics EXPRESS

Disclosures. The authors declare no conflicts of interest.

Data availability. Data underlying the results presented in this paper are not publicly available at this time but may be obtained from the authors upon reasonable request.

References

1. Y. Sun and H. Jiang, "Enhancing finite element-based photoacoustic tomography by localized reconstruction method," Photonics **9**(5), 337 (2022).
2. M. Shi, T. Vercauteren, and W. Xia, "Learning-based sound speed estimation and aberration correction for linear-array photoacoustic imaging," Photoacoustics **38**, 100621 (2024).
3. W. Choi, D. Oh, and C. Kim, "Practical photoacoustic tomography: Realistic limitations and technical solutions," J. Appl. Phys. **127**(23), 230903 (2020).
4. J. Li, C. Wang, T. Chen, *et al.*, "Deep learning-based quantitative optoacoustic tomography of deep tissues in the absence of labeled experimental data," Optica **9**(1), 32–41 (2022).
5. Y. Wen, Y. Huang, L. Huang, *et al.*, "Photoacoustic/ultrasound dual-modal imaging of human nails: a pilot study," J. Innov. Opt. Health Sci. **17**(06), 1 (2024).
6. S. Wang, B. Huang, S. C. K. Chan, *et al.*, "Tri-modality *in vivo* imaging for tumor detection with combined ultrasound, photoacoustic, and photoacoustic elastography," Photoacoustics **38**, 100630 (2024).
7. S.-Z. Xu, S.-M. Xie, D. Wu, *et al.*, "Ultrasound/photoacoustic dual-modality imaging based on acoustic scanning galvanometer," ACTA Phys. Sin. **71**(5), 050701 (2022).
8. T. Zhang, H. Guo, W. Qi, *et al.*, "Wearable photoacoustic watch for humans," Opt. Lett. **49**(6), 1524–1527 (2024).
9. Y. Li, F. Ye, S. Zhang, *et al.*, "Carbon-coated magnetic nanoparticle dedicated to MRI/photoacoustic imaging of tumor in living mice," Front. Bioeng. Biotechnol. **9**, 800744 (2021).
10. B. Wang, X. Zhang, L. Zhang, *et al.*, "Investigation of transducer distribution in compressive thermoacoustic tomography for breast cancer detection," IEEE Sens. J. **24**(1), 788–797 (2024).
11. B. Park, D. Oh, J. Kim, *et al.*, "Functional photoacoustic imaging: from nano- and micro- to macro-scale," Nano Converg. **10**(1), 29 (2023).
12. T. Jin, W. Qi, X. Liang, *et al.*, "Photoacoustic imaging of brain functions: wide field-of-view functional imaging with high spatiotemporal resolution (vol 16, 2100304, 2022)," Laser Photonics Rev. **17**(4), 2300067 (2023).
13. R. Ni, X. L. Deán-Ben, V. Treyer, *et al.*, "Coregistered transcranial optoacoustic and magnetic resonance angiography of the human brain," Opt. Lett. **48**(3), 648–651 (2023).
14. Y. Xie, D. Wu, X. Wang, *et al.*, "Image enhancement method for photoacoustic imaging of deep brain tissue," in *Photonics* (MDPI, 2023), 11(1), p. 31.
15. Y. Wang, L. Li, W. Qi, *et al.*, "Non-telecentric photoacoustic microscopy for multi-scale imaging," Opt. Lett. **49**(10), 2637–2640 (2024).
16. H. Jin, Z. Zheng, Z. Cui, *et al.*, "A flexible optoacoustic blood 'stethoscope' for noninvasive multiparametric cardiovascular monitoring," Nat. Commun. **14**(1), 4692 (2023).
17. Z. Huang, S. Mo, H. Wu, *et al.*, "Optimizing breast cancer diagnosis with photoacoustic imaging: an analysis of intratumoral and peritumoral radiomics," Photoacoustics **38**, 100606 (2024).
18. G. Li, Z. Huang, H. Tian, *et al.*, "Deep learning combined with attention mechanisms to assist radiologists in enhancing breast cancer diagnosis: a study on photoacoustic imaging," Biomed. Opt. Express **15**(8), 4689–4704 (2024).
19. J. Rodrigues, A. Amin, S. Chandra, *et al.*, "Machine learning enabled photoacoustic spectroscopy for noninvasive assessment of breast tumor progression *in vivo* : a preclinical study," ACS Sens. **9**(2), 589–601 (2024).
20. A. F. Kukk, F. Scheling, R. Panzer, *et al.*, "Combined ultrasound and photoacoustic C-mode imaging system for skin lesion assessment," Sci. Rep. **13**(1), 17947 (2023).
21. A. F. Kukk, F. Scheling, R. Panzer, *et al.*, "Non-invasive 3D imaging of human melanocytic lesions by combined ultrasound and photoacoustic tomography: a pilot study," Sci. Rep. **14**(1), 2768 (2024).
22. D. Li, Y. Yao, T. Zuo, *et al.*, "In vivo structural and functional imaging of human nailbed microvasculature using photoacoustic microscopy," Opt. Lett. **48**(21), 5711–5714 (2023).
23. R. Prakash, R. Manwar, and K. Avanaki, "Evaluation of 10 current image reconstruction algorithms for linear array photoacoustic imaging," J. Biophotonics **17**(3), e202300117 (2024).
24. S. Paul, A. Thomas, and M. S. Singh, "Delay-and-sum-to-delay-standard-deviation factor: a promising adaptive beamformer," Opt. Lett. **46**(18), 4662–4665 (2021).
25. S. Paul, S. Mulani, N. Daimary, *et al.*, "Simplified-delay-multiply-and-sum-based promising beamformer for real-time photoacoustic imaging," IEEE Trans. Instrum. Meas. **71**, 1–9 (2022).
26. S. Cho, S. Jeon, W. Choi, *et al.*, "Nonlinear pth root spectral magnitude scaling beamforming for clinical photoacoustic and ultrasound imaging," Opt. Lett. **45**(16), 4575–4578 (2020).
27. C. G. Hoelen and F. F. de Mul, "Image reconstruction for photoacoustic scanning of tissue structures," Appl. Opt. **39**(31), 5872–5883 (2000).
28. V. Perrot, M. Polichetti, F. Varray, *et al.*, "So you think you can DAS? A viewpoint on delay-and-sum beamforming," Ultrasonics **111**, 106309 (2021).
29. S. Paul, S. Mandal, and M. S. Singh, "Noise adaptive beamforming for linear array photoacoustic imaging," IEEE Trans. Instrum. Meas. **70**, 1–11 (2021).

Biomedical Optics EXPRESS

30. M. Mozaffarzadeh, Y. Yan, M. Mehrmohammadi, *et al.*, "Enhanced linear-array photoacoustic beamforming using modified coherence factor," J. Biomed. Opt. **23**(02), 1–026005 (2018).
31. S. Paul, S. Mulani, M. K. A. Singh, *et al.*, "Improvement of LED-based photoacoustic imaging using lag-coherence factor (LCF) beamforming," Med. Phys. **50**(12), 7525–7538 (2023).
32. G. Matrone, A. S. Savoia, G. Caliano, *et al.*, "The delay multiply and sum beamforming algorithm in ultrasound B-mode medical imaging," IEEE Trans. Med. Imaging **34**(4), 940–949 (2015).
33. M. Mozaffarzadeh, A. Mahloojifar, M. Orooji, *et al.*, "Double-stage delay multiply and sum beamforming algorithm: application to linear-array photoacoustic imaging," IEEE Trans. Biomed. Eng. **65**(1), 31–42 (2018).
34. T. Kirchner, F. Sattler, J. Gröhl, *et al.*, "Signed real-time delay multiply and sum beamforming for multispectral photoacoustic imaging," J. Imaging **4**(10), 121 (2018).
35. S. Jeon, E.-Y. Park, W. Choi, *et al.*, "Real-time delay-multiply-and-sum beamforming with coherence factor for *in vivo* clinical photoacoustic imaging of humans," Photoacoustics **15**, 100136 (2019).
36. S. Mulani, S. Paul, and M. S. Singh, "Higher-order correlation based real-time beamforming in photoacoustic imaging," J. Opt. Soc. Am. A **39**(10), 1805–1814 (2022).
37. Q. Mao, W. Zhao, X. Qian, *et al.*, "Improving photoacoustic imaging in low signal-to-noise ratio by using spatial and polarity coherence," Photoacoustics **28**, 100427 (2022).
38. R. Al Mukaddim, R. Ahmed, and T. Varghese, "Subaperture processing-based adaptive beamforming for photoacoustic imaging," IEEE Trans. Ultrason., Ferroelect., Freq. Contr. **68**(7), 2336–2350 (2021).
39. S. Park, A. B. Karpiouk, S. R. Aglyamov, *et al.*, "Adaptive beamforming for photoacoustic imaging," Opt. Lett. **33**(12), 1291–1293 (2008).
40. M. A. L. Bell, X. Guo, H. J. Kang, *et al.*, "Improved contrast in laser-diode-based photoacoustic images with short-lag spatial coherence beamforming," in *2014 IEEE International Ultrasonics Symposium* (IEEE, 2014), pp. 37–40.
41. M. A. Lediju Bell, N. Kuo, D. Y. Song, *et al.*, "Short-lag spatial coherence beamforming of photoacoustic images for enhanced visualization of prostate brachytherapy seeds," Biomed. Opt. Express **4**(10), 1964–1977 (2013).
42. E. A. Gonzalez, A. Jain, and M. A. L. Bell, "Combined ultrasound and photoacoustic image guidance of spinal pedicle cannulation demonstrated with intact ex vivo specimens," IEEE Trans. Biomed. Eng. **68**(8), 2479–2489 (2021).
43. G. S. Fernandes, J. H. Uliana, L. Bachmann, *et al.*, "Mitigating skin tone bias in linear array in vivo photoacoustic imaging with short-lag spatial coherence beamforming," Photoacoustics **33**, 100555 (2023).
44. J. Tordera Mora, X. Feng, N. Nyayapathi, *et al.*, "Generalized spatial coherence reconstruction for photoacoustic computed tomography," J. Biomed. Opt. **26**(04), 046002 (2021).
45. R. Al Mukaddim and T. Varghese, "Spatiotemporal coherence weighting for in vivo cardiac photoacoustic image beamformation," IEEE Trans. Ultrason., Ferroelect., Freq. Contr. **68**(3), 586–598 (2020).
46. J.-F. Synnevag, A. Austeng, and S. Holm, "Benefits of minimum-variance beamforming in medical ultrasound imaging," IEEE Trans. Ultrason., Ferroelect., Freq. Contr. **56**(9), 1868–1879 (2009).
47. Y. Wang, Y. Wang, M. Liu, *et al.*, "Minimum variance beamforming combined with covariance matrix-based adaptive weighting for medical ultrasound imaging," Biomed. Eng. OnLine **21**(1), 40 (2022).
48. B. E. Treeby and B. T. Cox, "k-Wave: MATLAB toolbox for the simulation and reconstruction of photoacoustic wave fields," J. Biomed. Opt. **15**(2), 021314 (2010).
49. S. Hakakzadeh, M. Amjadian, Y. Zhang, *et al.*, "Signal restoration algorithm for photoacoustic imaging systems," Biomed. Opt. Express **14**(2), 651–666 (2023).